ORIGINAL ARTICLE

Journal Section

# Teleconnection and the Antarctic response to the Indian Ocean Dipole in CMIP5 and CMIP6 models

**Arnab Sen[1] | Pranab Deb[1] | Adrian J. Matthews[2] | Manoj M. Joshi[3]**

[1]Centre for Ocean, River, Atmosphere and Land Sciences (CORAL), Indian Institute of Technology Kharagpur, Kharagpur, India

[2]Centre for Ocean and Atmospheric Sciences, School of Environmental Sciences and School of Mathematics, University of East Anglia, Norwich, United Kingdom

[3]Climatic Research Unit and Centre for Ocean and Atmospheric Sciences, School of Environmental Sciences, University of East Anglia, Norwich, United Kingdom

**Correspondence**
P. Deb, Centre for Ocean, River, Atmosphere and Land Sciences (CORAL), Indian Institute of Technology Kharagpur, Kharagpur, India
Email: pranab@coral.iitkgp.ac.in

**Funding information**
Indian Institute of Technology Kharagpur

Tropical-Antarctic teleconnections are known to have large impacts on Antarctic climate variability at multiple timescales. Anomalous tropical convection triggers upper-level quasi-stationary Rossby waves, which propagate to high southern latitudes and impact the local environment. Here the teleconnection between the Indian Ocean Dipole (IOD) and Antarctica was examined using daily gridded reanalysis data and the Linear Response Theory Method (LRTM) during September–November of 1980–2015. The individual contribution of the IOD over the Antarctic climate is challenging to quantify as positive IOD events often co-occur with El Niño events. However, using the LRTM, the extratropical response due to a positive IOD was successfully extracted from the combined signal in the composite map of anomalous 250-hPa geopotential height. Applying the method to a set of models from phase 5 and 6 of the Coupled Model Intercomparison Project (CMIP5 and CMIP6), significant differences were observed in the extratropical response to the IOD among the models due to bias in Rossby waveguide and IOD precipitation pattern. The LRTM was then applied to evaluate the extratropical response of the 850-hPa temperature, wind anomalies, and sea ice concentration anomalies in observation data, and models that adequately represented both the IOD precipitation and the extratropical waveguide. The IOD-induced cold southerly flow over the west of the Ross Sea, the Weddell Sea, and the Antarctic Peninsula, causing cold surface temperature anomalies and the increase of sea ice, and warm northerly flow over the east of the Ross Sea and the Amundsen Sea, causing warm surface temperature anomalies and the decrease of sea ice. We recommend the LRTM as a complementary method to standard analysis of climate variability from observations and global climate models.

Keywords : Tropical-Antarctic teleconnections, Rossby waves, IOD, CMIP5, CMIP6, Sea ice.

# 1 | INTRODUCTION

Over recent decades, the Antarctic region has experienced substantial climatic change (Turner et al. 2005; Stokes et al. 2022) which includes the rise of surface air temperature over West Antarctica and the Antarctic Peninsula (Bromwich et al. 2013; Johnson et al. 2022), the increase of ocean heat content and subsurface ocean temperature (Domingues et al. 2008; Spence et al. 2014), and rapid reduction in sea ice cover after 2015 (Turner et al. 2017; Parkinson 2019). Warm air temperatures cause intense surface melting (Kuipers Munneke et al. 2018; Johnson et al. 2022; Orr et al. 2023) and the formation of meltwater ponds over the ice shelves during summer (Dell et al. 2020; Banwell et al. 2021). The surface melting along with the intrusion of warm water from below (Pritchard et al. 2012) has caused thinning of floating ice shelves in recent decades (Paolo et al. 2015), which in turn causes accelerated mass loss from the ice sheet, consequently accelerating sea level rise (Pritchard et al. 2012; Rignot et al. 2019). These recent changes are attributed to several factors, such as the shift of the Southern Annular Mode (SAM) to a more positive phase driven by increased emissions of greenhouse gas and loss of stratospheric ozone (Thompson et al. 2011; Jones et al. 2019), and anthropogenic warming (Arblaster and Meehl 2006).

Tropical-Antarctic teleconnections have also been found to be important for understanding recent climatic changes around Antarctica (Yuan et al. 2018; Li et al. 2021; Orr et al. 2023). Tropical Sea Surface Temperature (SST) variability modulates the Antarctic climate through Rossby wave dynamics (Li et al. 2021). Deep convection in the tropics produces anomalous mid-tropospheric diabetic heating and forms local Hadley circulation, associated with divergence at the upper troposphere and anomalous convergence and sinking motion in the subtropics. The upper-level convergence in the subtropics and the presence of westerlies, especially the subtropical jet, generate an upper-level vorticity source known as the Rossby wave source (Sardeshmukh and Hoskins 1988). This wave source excites the wave train, which propagates to the southern high latitudes and influences the local climate (Ding and Steig 2013; Simpkins et al. 2016). For example, SST anomalies associated with the El Nino-Southern Oscillation (ENSO) have been linked to anomalous patterns of sea ice and surface temperature across the Antarctic Peninsula, known as the Antarctic Dipole (Yuan and Martinson 2001; Yuan 2004). Recent studies have demonstrated the role of the Interdecadal Pacific Oscillation and the South Pacific convergence zone in modulating sea level pressure and surface wind fields around Antarctica (Meehl et al. 2016; Clem et al. 2020). Atlantic Multidecadal variability contributes to Antarctic Peninsula warming by reducing the surface pressure in the Amundsen Sea (Li et al. 2014; Simpkins et al. 2014). SST anomalies over the tropical Indian Ocean have also been found to have significantly contributed to sea ice changes around Antarctica (Purich and England 2019; Wang et al. 2019; Yu et al. 2022).

The Indian Ocean Dipole (IOD) (Saji et al. 1999; Webster et al. 1999) is one of the major modes of tropical Indian Ocean SST variability, peaking in September-November (Saji and Yamagata 2003; Zhao and Hendon 2009). The positive phase of the IOD is characterized by anomalous cool SSTs over the eastern equatorial Indian Ocean with suppressed atmospheric convection, lower sea level, and a shallower thermocline, and anomalously warm SSTs over the western equatorial Indian Ocean with enhanced atmospheric convection, higher sea level, and a deeper thermocline. Recent studies have identified the impact of a positive IOD on Antarctic sea ice variability. Using singular value decomposition, Nuncio and Yuan (2015), found that the impact of the IOD is strong in the Indian Ocean sector, west of the Ross Sea, and in the central Pacific sector of Antarctica. They noticed wave train forced by IOD generates anomalous high and low pressure centres close to the Antarctic sea ice zone. The northward (southward) flow associated with those anomalous pressure centres was found responsible for sea ice growth (decay) near $60^0$E ($90^0$E) and west of the Ross Sea region. Feng et al. 2019, noticed positive and negative geopotential height anomaly centres at 500-hPa, close to the sea ice region of Antarctica during the strong positive IOD years due to Rossby wave activity flux. By computing the partial correlation coefficients, they noticed sea ice increase (decrease) due to northward (southward) wind anomalies due to IOD. However, positive IOD events mostly co-occur with El Niño events (Annamalai et al. 2005; Luo et al. 2010) making it difficult to isolate and quantify the extratropical impact of the IOD itself. Therefore, despite considerable progress in understanding the influence of the IOD over the Antarctic climate, a robust quantification of IOD response in the Southern Hemisphere is lacking. Moreover, a systematic evaluation of IOD-Antarctic teleconnection in the phase 5 and 6 of the Coupled Model Intercomparison Project (CMIP5 and CMIP6) ensembles is yet to be done, and hence the potential impact of the IOD on Antarctica in future climate scenarios is also unknown.

This paper aims to constrain the extratropical response to the positive IOD using reanalysis datasets and a semi empirical Linear Response Theory Method (LRTM). Further, we aim to identify biases and uncertainties in the IOD-Antarctic teleconnection in state-of-the-art General Circulation Models (GCMs) in the context of stationary Rossby wave theory. The rest of the paper is organized as follows. Section 2 provides the description of datasets and methods used. Tropical forcing due to the IOD and subsequent extratropical linear response over the Southern Hemisphere are presented in Section 3. CMIP biases are examined in sections 4 and 5 and CMIP classification is presented in section 6. In section 7, the fidelity of the best-performing model's ensemble in representing the IOD influence on low-level temperature and wind fields and sea ice concentration around Antarctica is presented. Finally conclusions are drawn in section 8.

## 2 | DATA AND METHOD

The Dipole Mode Index (DMI) (Saji et al. 1999), defined as the difference in SST anomalies between the tropical western Indian Ocean ($50^0$E - $70^0$E, $10^0$S - $10^0$N) and the tropical eastern Indian Ocean ($90^0$E - $110^0$E, $10^0$S - Equator), was used to identify the IOD. A mean September-October-November (SON) DMI value higher than 1 standard deviation above the mean was chosen as the threshold to identify positive IOD years.

The extratropical linear response to a positive IOD event was quantified using the LRTM technique, demonstrated by Deb et al. (2020). The LRTM represents the signal $S$ at time $t$ (days) as the weighted sum of the lagged forcing $F$ for the last $T$ days. Mathematically it can be written as

$$S(t) = \int_0^T G(\tau)F(t-\tau)d\tau + \in, \tag{1}$$

where $G$ is the Green's function, which is evaluated by the linear least square regression between signal and lagged forcing (Kostov et al. 2017), $\tau$ represents lag, and $\in$ is the nonlinear residual term. Here, the signal $S$ is the anomalous geopotential height at 250-hPa over the Southern Hemisphere midlatitudes, and forcing $F$ is the tropical forcing related to positive IOD.

Using $G$, the step response is computed at time lag $\tau_j$ as follows:

$$S_{step}(\tau_j) \approx \sum_{i=0}^{j} G(\tau_i)\Delta\tau \, . \tag{2}$$

In this study, $\Delta\tau$ represents the time interval of the data, which is one day. The quasi-stationary step responses are averaged over a lag of 30–40 days, with the resulting average response being considered as the extratropical linear response to anomalous positive IOD precipitation .

To identify the propagation path of Rossby waves, total stationary Rossby wavenumber $K_s$ is computed (Hoskins and Ambrizzi 1993; Dawson et al. 2011) by:

$$K_s = \sqrt{\frac{\beta - \bar{u}_{yy}}{\bar{u}}}, \tag{3}$$

where $\beta$ is meridional gradient of planetary vorticity, $\bar{u}_{yy}$ is the time mean meridional gradient of relative vorticity, and $\bar{u}$ is zonal wind climatology.

Daily geopotential height, temperature, eastward wind (U-wind), northward wind (V-wind), and monthly U-wind datasets were taken from NCEP/DOE reanalysis II (Kanamitsu et al. 2002). The daily sea ice concentration dataset was taken from the National Snow and Ice Data Center (NSIDC) version 4, applying the Bootstrap Algorithm (Meier et al. 2021). Monthly SST data was taken from Hadley Center Sea Ice and Sea Surface Temperature version 1.1 (HadISST 1.1) (Rayner et al. 2003). The daily precipitation dataset was obtained after linear interpolating the CMAP pentad precipitation dataset (Xie and Arkin 1997). While daily gridded precipitation fields are ideal for calculating the LRTM forcing, the significant impact on extratropical circulation is expected only from consistent precipitation anomalies, resolvable by pentad-mean datasets. To test this hypothesis, we computed the step response due to forcing calculated using European Centre for Medium-Range Weather Forecasts (ECMWF) fifth generation atmospheric reanalysis (ERA5) (Hersbach et al. 2020) daily precipitation (Not shown). The resulting step response closely matches our result, indicating that the interpolation had negligible impact on the results presented in this study. All datasets were examined for the 1980-2015 period.

Outputs from 19 CMIP5 (Taylor et al. 2012) and 21 CMIP6 (Eyring et al. 2016) historical simulations were considered for this study. For each of the CMIP models, only one ensemble member (r1i1p1 for CMIP5 and mostly r1i1p1f1 for CMIP6 with the variant f2 for a few models) were used. Daily datasets were used for the variables like precipitation, geopotential height, temperature, U and V winds, and sea ice area fraction. Monthly datasets include SST and U-wind. CMIP5 datasets were used for the 1980-2005 period and CMIP6 datasets were used for the 1980-2014 period. No significant changes in the results were observed when NCEP/DOE Reanalysis II datasets and CMIP6 datasets were analyzed for the 1980–2005 period (Not shown).

A Fourier filtering method was employed to compute daily anomalies. This filtering technique effectively removed the annual cycle, which includes the time mean and the first six annual harmonics. Linear detrending was applied to all the datasets to remove the effect of longer-term effects such as anthropogenic forcing, leaving interannual variability.

# 3 | EXTRATROPICAL LINEAR RESPONSE DUE TO POSITIVE IOD

## 3.1 | Observations

Positive IODs are often associated with El Niño events which makes it extremely difficult to isolate the extratropical response due to IOD alone. For example, the composite map (Figure 1a) of anomalous precipitation for positive IOD SON seasons between 1980 and 2015 shows anomalously positive precipitation over the tropical western Indian Ocean and anomalously negative precipitation over the tropical eastern Indian Ocean. This is the IOD signal (Saji et al. 1999). However, there is also anomalously positive precipitation over the tropical eastern Pacific, and anomalously negative precipitation over the tropical western Pacific and Maritime Continent, which is an El Niño signal.

The substantial anomalous precipitation dipole associated with the IOD is mainly located over the region ($50^0$E - $100^0$E, $10^0$S - $5^0$N) bounded by the green box in Figure 1a. To prepare the tropical forcing related to positive IOD for the LRTM technique, a similarity metric $\sigma(t_j)$ for each time $t_j$ was prepared, following Deb et al. (2020). The similarity metric was calculated by computing the inner product between the composite map $A$ of precipitation anomaly and the daily map $B(t_j)$ of anomalous precipitation, over the region bounded by the green box in Figure 1a.

$$\sigma(t_j) = A.B(t_j)\ . \tag{4}$$

Hence, the similarity metric is a daily time series for SON during 1980–2015 with high positive values representing higher similarity (in terms of pattern and magnitude) with anomalous positive IOD precipitation pattern. The days corresponding to the upper quartile values of the similarity metric were identified, and the composite map for these upper quartile days was prepared (Figure 1b). The similarity metric effectively removed most of the El Niño related precipitation anomaly from the tropical Pacific, thus successfully isolating the IOD signal.

The linear step response in the Southern Hemisphere extratropics to the positive IOD was then computed. Using Equation 1, the forcing $F(t)$ was taken to be the time series of the similarity metric $\sigma(t_j)$ from Equation 4, and the signal $S(t)$ was the 250-hPa geopotential height at any particular grid point. The step response $S_{step}(\tau)$ (Equation 2) of the 250-hPa geopotential height was then calculated using the resulting Green's function, which was then averaged over lag 30–40 days to estimate the quasi-stationary response. This process was carried out for 250-hPa geopotential height at every grid point, and plotted as a map in Figure 2a. A series of positive and negative anomaly centres are located around Antarctica. Starting from the Indian Ocean, the wave train reaches southern Australia, west of Ross Sea and closer to Antarctic Peninsula before entering the Atlantic region. The wave train then travels further before decaying. The LRTM successfully isolated the individual upper tropospheric response over the extratropics of the Southern Hemisphere due to the positive IOD alone, from the combined signal due to the positive IOD plus El Niño that is present in the composite map Figure 2b. The extratropical linear Rossby wave pattern in Figure 2a is similar to the spatial pattern of partial correlation coefficients between DMI and 500-hPa geopotential height anomalies during austral spring, as demonstrated in Feng et al.(2019), independently validating the LRTM methodology. As the geopotential height anomaly centres are located close to the Antarctic region, they are likely to play an important role in modulating the local weather by anomalous meridional advection of heat and moisture towards and away from the Antarctic continent.

## 3.2 | CMIP5 Models

We next employed the LRTM to evaluate the performance of 19 CMIP5 models in capturing the IOD-Antarctic teleconnection. For each model, we identified the positive IOD years to prepare the individual tropical forcing. An analysis of the results reveals a substantial intermodel spread in the linear extratropical response to the positive IOD, as illustrated in Figure S1. Notably, when compared to the reference Figure 2a, all the models exhibited biases in representing the magnitudes and locations of the anomaly centres. To enable a robust comparison between observed and simulated IOD responses, the study first identified the observed Rossby wave path originating at $72.5^0$E and $35^0$S, which followed the maxima and minima of the anomaly centres of the step response map depicted in Figure 2a. Next, we computed the meridionally averaged step response (over a 1000 km meridional distance) at each longitude along this path. This allowed us to generate the magnitude along the observed Rossby wave path for the step response map from the observation data. To ensure comparability, we remapped the step response map of each CMIP5 model onto a regular grid of $2.5^0 \times 2.5^0$, same as the observation grid. Following that, we computed the meridionally averaged step response along the same observed Rossby wave path for each CMIP5 model's step response map.

The comparison in Figure 3a reveals that, in the subtropical Indian Ocean (centered at $72.5^0$E, $35^0$S), the multi-model mean of the step responses is indistinguishable from zero. The observed step response falls outside the multi-model range. A few models (e.g., CMCC-CM, CMCC-CMS, IPSL-CM5A-MR, MIROC5) exhibit an opposite sign for the response, deviating from the observed negative anomaly response. Given the considerable inaccuracies displayed by the models in capturing the initial location and magnitude of the anomaly centre as the wave train initiates into the extratropical region, their capacity to adequately portray the overall response across the extratropics will likely be constrained.

For the positive anomaly response located south of Australia (centered at $120^{0}$E, $42.5^{0}$S), the multi-model mean of the step responses exhibits a similar positive sign to observation. However, most models, including the multi-model mean, underestimate the magnitude of the anomaly centre. The observed step response lies outside the one standard deviation band, suggesting the majority of the models' inability to simulate the location and magnitude of the centre adequately.

Focusing on the negative anomaly centre located at $177.5^{0}$W, $55^{0}$S, the multi-model mean of the step responses exhibits a similar negative sign as observation. However, the observed step response lies beyond the collective range of models, indicating a consistent underestimation of the centre's magnitude by all models. A few models (e.g., GFDL-ESM2G, HadCM3, MPI-ESM-MR) exhibit an opposite sign for the response, deviating from the observed negative anomaly response.

Subsequently, the prominent positive response observed over the Amundsen Sea (centre located at $112.5^{0}$W, $65^{0}$S) was examined. The multi-model mean of the step responses exhibits a similar positive sign to observation. The observed step response falls within the one standard deviation range, signifying that most models effectively capture the anomaly centre. However, it's notable that a substantial number of models underestimate the magnitude of this centre. Conversely, a minority of models (e.g., CMCC-CM, HadCM3, MIROC5) exhibit a contrasting response, failing to replicate the observed positive anomaly seen over the Amundsen Sea.

Finally, the pronounced negative response over the Atlantic sector, centered at $30^{0}$W, $55^{0}$S, was analyzed. The multi-model mean of the step responses exhibits a similar negative sign to observation, albeit close to zero. However, the observed step response lies significantly outside the collective range represented by the models. This suggests a consistent tendency among all models to underestimate the magnitude of this centre. Specifically, several models (e.g., CNRM-CM5, HadCM3, HadGEM2-CC, HadGEM2-ES, IPSL-CM5A-MR) simulate an opposite sign for the response, indicating a discrepancy with the observed negative anomaly.

## 3.3 | CMIP6 Models

The LRTM was then employed to assess the performance of 21 CMIP6 models in capturing the IOD teleconnection. For each model, we identified the positive IOD years to prepare the individual tropical forcing. Similar to the CMIP5 models, a significant variation is observed among the CMIP6 models in their step response to the positive IOD, as depicted in Figure S2. The same evaluation technique used to assess the performance of CMIP5 models against observation was applied to evaluate the CMIP6 models. Figure 3b compares observation and CMIP6 models, focusing specifically on their capability to accurately represent the magnitude of the linear extratropical response to positive IOD. When compared to Figure 3a, the CMIP6 models were found to demonstrate similar characteristics to the CMIP5 models. Minor distinctions are evident for the negative anomaly response over the subtropical Indian Ocean (centered at $72.5^{0}$E, $35^{0}$S) and positive anomaly response over the south of Australia (centered at $120^{0}$E, $42.5^{0}$S). The multi-model mean of the step responses at $72.5^{0}$E, $35^{0}$S exhibits an opposite sign compared to the observation. In the case of CMIP5 models, the observed step response falls outside the one standard deviation range for the anomaly centre at $120^{0}$E, $42.5^{0}$S. However, for CMIP6 models, the observed step response falls within the one standard deviation range. Similar to CMIP5, the multi-model mean of CMIP6 models underestimates the magnitude of all anomaly centres. The overall performance of CMIP6 has not improved over CMIP5 in producing the extratropical response to positive IOD.

Accurate representation of the anomaly centres is crucial for understanding the influence of the IOD on Antarctic climate, as these centres play a significant role in modulating local weather patterns. Therefore, it is essential to correctly simulate the locations and magnitudes of these anomaly centres. To gain insights into the sources of biases exhibited by CMIP models in capturing this teleconnection, a thorough investigation into the dynamics of Rossby wave propagation is conducted in the subsequent section.

## 4 | STATIONARY ROSSBY WAVE PROPAGATION

The atmospheric basic state plays a crucial role in modulating the upper tropospheric circulation anomalies (Dawson et al. 2011; Deb et al. 2020). Here, the basic state of the CMIP models was evaluated using the stationary Rossby wavenumber diagnostic and the results were compared against the observation. Using Equation 3, the stationary Rossby wavenumber ($K_s$) was computed from the time mean zonal wind at 250 hPa. $K_s$ was used as the refractive index for Rossby waves, i.e., waves are refracted from lower values of $K_s$ towards higher values. Local maxima in the $K_s$ field were identified as Rossby waveguides.

In the observation (Figure 4a), a local maximum of $K_s$=4 is identified around 30$^0$S - 40$^0$S, extending across the Atlantic sector, continuing over the Indian and Pacific sectors, and finally returning to the Atlantic sector to complete the loop. Similarly, the local maxima of $K_s$=3 and 2 are evident around 60$^0$S, spreading across the different sectors, mirroring the pattern observed for $K_s$=4. During SON, these particular wavenumbers contribute to the formation of the waveguide in the extratropics. Within the waveguide, a negative step response initially emerges over the subtropical Indian Ocean (with its centre at 72.5$^0$E, 35$^0$S). Afterward, the wave train propagates following the waveguide and reaches the Pacific sector. It is reflected from the lower value of $K_s$ (west of the Antarctic Peninsula) and then refracts towards the higher value before decaying.

Bias in the Rossby waveguide structure changes the propagation path of Rossby waves (Dawson et al. 2011; Deb et al. 2020). We found significant bias in the waveguide structure in some of the models (GFDL-ESM2G, GFDL-ESM2M, IPSL-CM5A-MR, MIROC5, MIROC-ESM, MPI-ESM-MR, MRI-CGCM3, CNRM-CM6-1-HR, CNRM-ESM2-1, IITM-ESM) (as shown in Figure S3-S6). The incorrect representation of the waveguide causes the wave train to propagate in a different direction than observation and thus produces erroneous step responses in the models.

To quantify the CMIP bias in the Rossby waveguide, we remapped the stationary wavenumber map of each CMIP model onto a regular grid of 2.5$^0$ × 2.5$^0$, same as the observation grid. The wave train seen in observation (Figure 4a) and CMIP models have a zonal wavenumber of approximately 3, which can propagate in the region bounded by $K_s$=3 and 4. So, we computed the bias in the meridional location of $K_s$=2, 3, and 4 at each longitude. To do so, the meridional location at each longitude was noted for a particular wavenumber contour for both the observation and model. Then, the model bias in each longitude location was calculated in terms of the number of grids. This was done for all three wavenumber contours, and finally, the biases (for all the contours at all the longitudes) were added to obtain the total bias, which was then converted to degrees and zonally averaged to obtain average waveguide bias per longitude. The method was repeated for all the models, and each model's bias was noted (Figure 4b) which was further used for CMIP classification in section 6. It is to be noted that there are small islands of $K_s$=2, 3, and 4 within the region bounded by $K_s$=3 and 4 in both observation and models. However, as these islands have insignificant influence on the propagation of wave train, they were not included in the calculation of the waveguide bias.

## 5 | BIASES IN TROPICAL PRECIPITATION

Tropical forcing plays a vital role in tropical-Antarctic teleconnection studies. However, global climate models are prone to significant biases in mean surface zonal wind stress and SST (Lyu et al. 2020; McKenna et al. 2020). Both CMIP5 and CMIP6 models are known to exhibit double ITCZ bias and hence significant bias in tropical precipitation (Fiedler et al. 2020; Tian and Dong 2020). Li et al. (2015) analyzed a set of CMIP5 models and noticed an "IOD-like bias" pattern in precipitation over the tropical Indian Ocean. Recently, Long et al. (2020) identified "IOD-like biases" worsening from CMIP5 to CMIP6.

Composite maps of IOD precipitation anomaly for individual models reveal that the negative precipitation anomaly region is extended too far westward in some of the models (e.g., CMCC-CM, CMCC-CMS, CNRM-CM5, HadGEM2-CC, CESM2-WACCM-FV2, CNRM-CM6-1, CNRM-CM6-1-HR, CNRM-ESM2-1, FGOALS-f3-L, GFDL-ESM4, IITM-ESM, IPSL-CM6A-LR, UKESM1-0-LL) (as shown in Figures S7-S10). So, to quantify the bias in IOD precipitation pattern, we remapped each of the composite maps of anomalous IOD precipitation of the CMIP model onto a regular grid of $2.5^0 \times 2.5^0$, same as the observation grid. Then we calculated the east-west ratio, which is the ratio between the number of grid points containing positive anomaly values in the region encompassing $50^0$E - $75^0$E, $10^0$S - $5^0$N, and the number of grid points containing negative anomaly values in the region encompassing $75^0$E - $100^0$E, $10^0$S - $5^0$N (Figure 5a). The bias in the east-west ratio was computed by subtracting the ratio in the observation from the ratio in the model. The bias in east-west ratio represents the bias in the anomalous IOD precipitation pattern. The individual CMIP model biases in the IOD precipitation pattern is shown in Figure 5b. By employing this technique, we were able to distinguish the models that accurately captured the anomalous IOD precipitation pattern. Additionally, it facilitated the classification of models, as elaborated in the subsequent section.

## 6 | CMIP MODEL CLASSIFICATION

The biases present in global climate models have a notable impact on local climate variability and teleconnections with remote climate variability (Wang et al. 2014; Wang et al. 2017). Sections 4 and 5 of this study have reported significant biases in both CMIP5 and CMIP6 models concerning Rossby waveguides and IOD precipitation patterns. These biases may have impacted the IOD teleconnection in the respective models over the Southern Hemisphere. To assess the impact of these biases on model performance, the models were classified into four groups based on biases in waveguide structure and IOD precipitation pattern. Firstly, CMIP5 models were considered, and their arrangement in ascending order of waveguide bias allowed the determination of the median value. Similarly, the median value of IOD precipitation bias was determined. Models that exhibited biases lower than the median values in both waveguide and precipitation were classified as efficient in capturing these aspects and placed in class-A. A significant number of models demonstrated good representation of the extratropical waveguide but poor representation of the IOD precipitation pattern, leading to their placement in class-B. Models that poorly represented the extratropical waveguide but adequately represented the IOD precipitation pattern were assigned to class-C. The remaining models were classified as class-D. The model classification results are presented in Table 1, showcasing the variations in performance from CMIP5 to CMIP6 in capturing the waveguide and IOD precipitation pattern.

Out of the 19 CMIP5 models, only four models demonstrate efficient representation of both the Rossby waveguides and IOD precipitation patterns. However, in the case of CMIP6 models, a notable improvement is observed in the simulation of waveguides, with only one model falling into class-C (representing poor waveguide representation). Nevertheless, more CMIP6 models exhibit poor simulation of the IOD precipitation pattern compared to the CMIP5 models. This result aligns with the finding of Long et al. (2020), who reported a deterioration of IOD-like biases from CMIP5 to CMIP6.

Subsequently, we directed our attention towards evaluating the performance of each class in capturing the teleconnection associated with the positive IOD. To facilitate comparison with observation, the step response maps of each CMIP model were remapped onto a $2.5^0 \times 2.5^0$ regular grid. Furthermore, the multi-model mean of step responses was generated for each class, as depicted in Figures S11 and S12. The evaluation technique utilized in section 3 to assess the performance of individual CMIP responses was employed to evaluate the performance of the step responses for each class.

## 6.1 | CMIP5 classification

Figure 6 compares observation and different CMIP5 model classes regarding their ability to capture the magnitude of the linear extratropical response to positive IOD. The negative anomaly response over the subtropical Indian Ocean which is at the beginning of the wave train (centered at $72.5^0$E, $35^0$S) is reasonably captured by all the class-A models. In the case of class-D models, while the multi-model mean of the step responses shows similar sign as the observation, its magnitude approaches zero. Class-B exhibits zero multi-model mean, while class-C displays a positive mean. It is worth noting that all classes underestimate the magnitude of the centre, yet class-A demonstrates superior skill in capturing the magnitude of the anomaly centre.

Shifting our focus to the positive anomaly response to the south of Australia, centered at $120^0$E, $42.5^0$S, class-A stands out in simulating the anomaly centre most accurately, with both individual models and the multi-model mean of the step responses closely resembling the observed step response. Other classes manage to capture the centre's sign, albeit underestimating its magnitude. Interestingly, for class-D, the observed step response falls within the band of one standard deviation, suggesting better performance compared to classes-B and C in representing the anomaly centre.

Moving on to the negative anomaly response at $177.5^0$W, $55^0$S, the multi-model mean for classes-A, B, and D mirror the sign of the observed step response. However, the magnitude is almost zero for classes B and D. In all cases, the anomaly centre's magnitude is underestimated, yet class-A exhibits superior performance in reproducing the magnitude of the anomaly centre.

Examining the positive response over the Amundsen Sea at $112.5^0$W, $65^0$S, the multi-model mean in class-A closely matches the observed step response. Conversely, the other classes underestimate the anomaly centre's magnitude. Classes-C and D models are found to exhibit opposing signs.

Lastly, considering the negative anomaly response over the Atlantic sector, centered at $30^0$W, $55^0$S, the multi-model mean for classes-A and D displays the same sign as observation. Classes-B and C show zero multi-model mean values. Notably, all classes substantially underestimate the magnitude of the anomaly centre.

## 6.2 | CMIP6 classification

Figure 7 shows the performance comparison of various classes of CMIP6 models against observations. Comparing against Figure 6, we observe that the multi-model mean of CMIP6 class-A exhibits identical characteristics with the multi-model mean of CMIP5 class-A in simulating the magnitude of most of the anomaly centres. However, there are some distinct disparities. For example, the multi-model mean of CMIP5 class-A models exhibits a similar sign as the observed step response for the anomaly centre at $72.5^0$E, $35^0$S. However, the CMIP6 class-A multi-model mean is zero, and some CMIP6 class-A models even show opposite responses. These findings suggest that when it comes to accurately capturing the initial location and magnitude of the anomaly centre at the beginning of the wave train into the extratropics, the CMIP5 class-A models perform better compared to the CMIP6 class-A models. For the positive anomaly response over the Amundsen Sea (centered at $112.5^0$W, $65^0$S), the multi-model mean of CMIP5 class-A models closely aligns with the observed step response. In contrast, the CMIP6 class-A multi-model mean underestimates this magnitude.

Similar to CMIP5 class-A, the CMIP6 class-A outperforms the other classes in simulating the overall extratropical response to positive IOD. The comparison of multi-model step responses among different classes reveals that reducing biases in waveguides and IOD precipitation pattern substantially improves the model's ability to simulate the IOD teleconnection. The application of LRTM proved valuable in identifying CMIP biases related to teleconnection representation. In the subsequent section, we employed LRTM to quantitatively assess the impact of positive IOD on surface temperature and wind fields in the vicinity of Antarctica. This analysis was conducted using observational data and the CMIP5 and CMIP6 class-A ensembles.

## 7 | IMPACT OF IOD ON TEMPERATURE AND WIND FIELDS AND SEA ICE CONCENTRATION AROUND ANTARCTICA

The role of remote atmospheric variability over the surface temperature and wind fields around Antarctica has been studied extensively (Deb et al. 2018; Clem et al. 2019; Swetha Chittella et al. 2022; Orr et al. 2023). Recent studies have identified the impact of IOD on the Antarctic sea ice (Nuncio and Yuan 2015; Feng et al. 2019). Here we examine the role of IOD in modulating the temperature and wind fields at 850-hPa and sea ice concentration around Antarctica using LRTM.

Figure 8a and b show the linear step response at 850-hPa temperature and wind fields and sea ice concentration around Antarctica during SON for positive IOD years between 1980 and 2015, forced by the similarity metric computed in section 3. A series of anomalous cyclonic and anticyclonic circulations are noticed around Antarctica. The intense cyclonic circulation anomalies over the west Pacific and Atlantic sectors and the anticyclonic circulation anomaly over the Amundsen Sea region play a vital role in modulating the temperature anomalies around Antarctica. The anomalous cyclonic (anticyclonic) circulations are associated with cold southerly flow away from the Antarctic continent on the western (eastern) flank and warm northerly flow towards the Antarctic continent on the eastern (western) flank. The cold southerly flow over the Weddell Sea and to the west of the Ross Sea causes two intense negative temperature anomaly centres, causing anomalous sea ice increase to the west of the Ross Sea and over the Weddell Sea and the Bellingshausen Sea, surrounding the tip of the Antarctic Peninsula. In contrast, the warm northerly flow over the Amundsen and Ross Sea sectors causes a strong positive temperature anomaly centre, causing sea ice to melt. Our results support the findings of Nuncio and Yuan (2015), where similar anomaly centres around Antarctica were observed after partially regressing surface temperatures and wind fields onto the DMI. The anomalies were also found to be responsible for sea ice decay or growth. Feng et al. (2019) computed the partial correlation between the spring Antarctic sea ice and spring DMI. They noticed the spatial pattern of anomalous sea ice similar to our results.

Appreciating the performance of class-A models from CMIP5 and CMIP6, we evaluated their performance in capturing the IOD influence in the surface temperature and wind fields and sea ice concentration around Antarctica (Figure 8 (c-f)). Class-A from CMIP5 and CMIP6 simulate a weaker cyclonic circulation anomaly over the Weddell Sea. Both the class-A ensembles simulate a cooling effect over the Weddell Sea but with a reduced magnitude compared to the observation, causing the weak increase of sea ice. Class-A ensemble of CMIP5 performs better than class-A of CMIP6 in simulating the magnitude of the anticyclonic circulation anomaly over the Amundsen Sea sector and the cyclonic circulation anomaly over the west of Ross Sea. This result is consistent with the upper atmospheric responses for both the classes, where the class-A ensemble of CMIP5 performs better in capturing the magnitude of the anomaly centres compared to CMIP6. Both the class-A ensembles exhibit similar performance in simulating the sea ice concentration anomaly over the Amundsen Sea sector. However, only the class-A ensemble of CMIP5 simulates the positive sea ice concentration anomaly response over the west of Ross Sea, though the magnitude is weak compared to the observation.

## 8 | DISCUSSION AND CONCLUSIONS

Using the semi-empirical LRTM (Deb et al. 2020; Senapati et al. 2022), we investigate the IOD-Antarctic teleconnection during SON, 1980-2015. Quantifying the distinct impact of a positive IOD event on the Antarctic climate is challenging as positive IOD events mostly co-occur with El Niño. Employing the similarity metric, we could identify the days when the ENSO-related precipitation is minimal over the tropical Pacific and thus successfully eliminated most of the anomalous precipitation associated with El Niño from the IOD tropical forcing. Consequently, the LRTM method effectively isolates and captures the extratropical IOD signal over the Southern Hemisphere, disentangling it from the combined signal evident in the composite map. The extratropical response in geopotential height at 250-hPa shows a distinct Rossby wave train, characterized by a sequence of alternating high and low-pressure systems encircling Antarctica. This wave train originates in the subtropical Indian Ocean and extends its influence into both the Pacific and Atlantic sectors.

In our examination of extratropical responses to IOD forcing across a spectrum of CMIP5 and CMIP6 models, we uncover a substantial intermodel spread among these models in their capacity to accurately replicate both the spatial pattern and magnitude of this response. To identify the underlying source of this spread, we carried out a comprehensive assessment of the model simulated atmospheric basic state and IOD precipitation. The atmospheric basic state and waveguide for Rossby wave propagation were quantified using the stationary Rossby wavenumber diagnostic (Hoskins and Ambrizzi 1993; Dawson et al. 2011). Our analysis revealed large biases in the Rossby waveguide structure simulated by the CMIP models. An adequate representation of the IOD precipitation pattern is also crucial for Rossby wave teleconnection. We observed that most models poorly simulate the zonal asymmetric precipitation pattern during positive IOD events. This is in line with earlier studies that reported the presence of significant biases in the CMIP models in simulating tropical precipitation (Fiedler et al. 2020; Tian and Dong 2020), and 'IOD-like' biases in the atmospheric and oceanic variables over the tropical Indian Ocean (Li et al. 2015; Long et al. 2020). We observed significant improvement in the Rossby waveguide from CMIP5 to CMIP6. However, precipitation bias has increased from CMIP5 to CMIP6. To identify the relative impact of these biases on IOD-Antarctic teleconnection, the CMIP models were classified into four classes based on the biases in waveguide and IOD precipitation pattern.

The class-A models, i.e., models with adequate representation of the zonal asymmetric IOD precipitation pattern and Rossby waveguide, outperform other models in simulating the step responses. For class-B models, adequate representation of the waveguide sends Rossby waves in similar directions as observation. Still, their inability to adequately represent the IOD precipitation pattern hampers their capability to simulate step responses effectively. As for Class-C and D models, Rossby waves propagate differently than the observation due to inadequate representation of the waveguide. Consequently, these models yield incorrect step responses, even though Class-C models adequately represent the IOD precipitation pattern. These findings indicate the relative importance of the realistic representation of the atmospheric basic state and, hence, the Rossby waveguide over the IOD precipitation anomalies for better representation of the extratropical IOD responses in CMIP models.

Finally, we quantify the impact of IOD-teleconnection on Antarctic surface meteorological conditions using the LRTM. The IOD response in Antarctica was found to be associated with anomalous northerly (southerly) flow over the Amundsen and Ross Sea sector (the Weddell Sea sector and to the west of the Ross Sea). The warm northerly flow is associated with a warm temperature anomaly over the Amundsen and Ross Sea sectors. These temperature and wind anomalies are consistent with sea ice decrease (increase) over the Ross and Amundsen sea sectors (Bellingshausen and Weddell Sea sectors and west of Ross sea sector). The class-A ensemble demonstrates reasonable skill in capturing the observed wind, temperature, and sea ice concentration anomalies, even though the magnitude is weak compared to the observation. It is important to note that the class-A ensemble of CMIP5 demonstrates superior performance compared to the class-A ensemble of CMIP6 in simulating the magnitude of the anomaly centres around Antarctica. The decline in skill from CMIP5 to CMIP6 can be attributed to increased thermocline bias and resulting overly strong equatorial easterly wind in CMIP6 (Wang et al. 2021). Furthermore, CMIP6 models struggle to simulate the observed positive skewness of IOD, which has been identified as an important loss of realism in IOD simulation by McKenna et al. (2020).

Our study highlights the usefulness of LRTM in capturing the IOD impact on the Antarctic climate. Using this novel method, we identify critical biases within CMIP models in simulating the IOD-Antarctic teleconnection. We systematically identify the impact of inaccuracies in representing tropical forcing associated with IOD events, as well as deficiencies in modeling the Southern Hemisphere basic state. These biases collectively constrain the models' capacity to accurately quantify the impact of IOD-teleconnection on the Antarctic climate. It is important to highlight that employing the conventional partial correlation technique for calculating the extratropical IOD response based on SST indices (Feng et al. 2019) might not be appropriate for CMIP models due to climatological SST biases across the tropical Indian and Pacific oceans (McKenna et al. 2020). Also, partial correlation coefficients only provide the strength of the relationship between DMI and geopotential height anomalies, while LRTM quantifies the actual response. However, one caveat of the LRTM technique is its inability to capture nonlinear tropospheric and stratospheric processes due to its assumption of linearity. We recommend LRTM as a complementary technique along with the standard GCM experiments for future tropical-Antarctic teleconnection studies.

The outcome of this study is crucial against the backdrop of recent changes in Antarctic sea ice. Over the period spanning 1979 to 2015, Antarctic sea ice experienced notable growth, followed by a dramatic decline post-2015 (Stuecker et al. 2017; Meehl et al. 2019; Parkinson 2019). It is worth noting that the majority of the CMIP models struggle to accurately simulate the increasing trend (Turner et al. 2013; Shu et al. 2020). The inadequate representation of the tropical-Antarctic teleconnection in CMIP models could potentially limit their capacity to accurately depict changes in Antarctic sea ice. The frequency of IOD events has shown a marked increase in recent decades, and it is expected to increase further, in response to the projected global mean temperature rise (Cai et al. 2018; Sun et al. 2022). Consequently, the future evolution of Antarctic sea ice in both the Pacific and Atlantic sectors are likely to exhibit strong dependence on IOD-Antarctic teleconnection. Utilizing the LRTM approach, a follow-up study has been initiated to quantify future contributions of IOD events to surface temperature and sea ice patterns around Antarctica, relying on the top-performing CMIP models (classified as class-A) identified in our current study.

## ACKNOWLEDGEMENTS

We acknowledge the World Climate Research Programme and the climate modeling groups for producing and sharing the CMIP outputs, which can be accessed from https://esgf-index1.ceda.ac.uk/projects/esgf-ceda/. NSIDC dataset was downloaded from https://nsidc.org/data. NCEP/DOE Reanalysis II and CMAP datasets were downloaded from

NOAA PSL, Boulder, Colorado, USA, from their website at https://psl.noaa.gov. ERA5 dataset can be downloaded from https://cds.climate.copernicus.eu. The HadISST dataset was downloaded from the UK Met Office Hadley Centre, from their website at https://www.metoffice.gov.uk/hadobs/. AS and PD were supported by Indian Institute of Technology Kharagpur. We sincerely thank the anonymous reviewers whose valuable comments and suggestions helped to improve the readability of our paper.

## AUTHOR CONTRIBUTIONS

Arnab Sen: conceptualization; data curation; formal analysis; investigation; methodology; visualization; writing – original draft; writing – review and editing. Pranab Deb: conceptualization; methodology; supervision; writing – review and editing. Adrian J. Matthews: conceptualization; methodology; writing – review and editing. Manoj M. Joshi: conceptualization; methodology; writing – review and editing.

## CONFLICT OF INTEREST STATEMENT

The authors declare no conflict of interest.

## ORCID

Arnab Sen: https://orcid.org/0009-0007-0566-7786
Pranab Deb: https://orcid.org/0000-0002-1858-0918
Adrian J. Matthews: https://orcid.org/0000-0003-0492-1168
Manoj M. Joshi: https://orcid.org/0000-0002-2948-2811

## references

[1] Annamalai H, Xie S, McCreary J, Murtugudde R. Impact of Indian Ocean sea surface temperature on developing El Niño. Journal of Climate 2005;18(2):302–319.

[2] Arblaster JM, Meehl GA. Contributions of external forcings to southern annular mode trends. Journal of climate 2006;19(12):2896–2905.

[3] Banwell AF, Datta RT, Dell RL, Moussavi M, Brucker L, Picard G, et al. The 32-year record-high surface melt in 2019/2020 on the northern George VI Ice Shelf, Antarctic Peninsula. The Cryosphere 2021;15(2):909–925.

[4] Bromwich DH, Nicolas JP, Monaghan AJ, Lazzara MA, Keller LM, Weidner GA, et al. Central West Antarctica among the most rapidly warming regions on Earth. Nature Geoscience 2013;6(2):139–145.

[5] Cai W, Wang G, Gan B, Wu L, Santoso A, Lin X, et al. Stabilised frequency of extreme positive Indian Ocean Dipole under 1.5 C warming. Nature communications 2018;9(1):1419.

[6] Clem KR, Fogt RL, Turner J, Lintner BR, Marshall GJ, Miller JR, et al. Record warming at the South Pole during the past three decades. Nature Climate Change 2020;10(8):762–770.

[7] Clem KR, Lintner BR, Broccoli AJ, Miller JR. Role of the South Pacific convergence zone in West Antarctic decadal climate variability. Geophysical Research Letters 2019;46(12):6900–6909.

[8] Dawson A, Matthews AJ, Stevens DP. Rossby wave dynamics of the North Pacific extra-tropical response to El Niño: Importance of the basic state in coupled GCMs. Climate dynamics 2011;37:391–405.

[9] Deb P, Matthews AJ, Joshi MM, Senior N. The extratropical linear step response to tropical precipitation anomalies and its use in constraining projected circulation changes under climate warming. Journal of Climate 2020;33(16):7217–7231.

[10] Deb P, Orr A, Bromwich DH, Nicolas JP, Turner J, Hosking JS. Summer drivers of atmospheric variability affecting ice shelf thinning in the Amundsen Sea Embayment, West Antarctica. Geophysical Research Letters 2018;45(9):4124–4133.

[11] Dell R, Arnold N, Willis I, Banwell A, Williamson A, Pritchard H, et al. Lateral meltwater transfer across an Antarctic ice shelf. The Cryosphere 2020;14(7):2313–2330.

[12] Ding Q, Steig EJ. Temperature change on the Antarctic Peninsula linked to the tropical Pacific. Journal of Climate 2013;26(19):7570–7585.

[13] Domingues CM, Church JA, White NJ, Gleckler PJ, Wijffels SE, Barker PM, et al. Improved estimates of upper-ocean warming and multi-decadal sea-level rise. Nature 2008;453(7198):1090–1093.

[14] Eyring V, Bony S, Meehl GA, Senior CA, Stevens B, Stouffer RJ, et al. Overview of the Coupled Model Intercomparison Project Phase 6 (CMIP6) experimental design and organization. Geoscientific Model Development 2016;9(5):1937–1958.

[15] Feng J, Zhang Y, Cheng Q, San Liang X, Jiang T. Analysis of summer Antarctic sea ice anomalies associated with the spring Indian Ocean dipole. Global and Planetary Change 2019;181:102982.

[16] Fiedler S, Crueger T, D'Agostino R, Peters K, Becker T, Leutwyler D, et al. Simulated tropical precipitation assessed across three major phases of the Coupled Model Intercomparison Project (CMIP). Monthly Weather Review 2020;148(9):3653–3680.

[17] Hersbach H, Bell B, Berrisford P, Hirahara S, Horányi A, Muñoz-Sabater J, et al. The ERA5 global reanalysis. Quarterly Journal of the Royal Meteorological Society 2020;146(730):1999–2049.

[18] Hoskins BJ, Ambrizzi T. Rossby wave propagation on a realistic longitudinally varying flow. Journal of Atmospheric Sciences 1993;50(12):1661–1671.

[19] Johnson A, Hock R, Fahnestock M. Spatial variability and regional trends of Antarctic ice shelf surface melt duration over 1979–2020 derived from passive microwave data. Journal of Glaciology 2022;68(269):533–546.

[20] Jones ME, Bromwich DH, Nicolas JP, Carrasco J, Plavcová E, Zou X, et al. Sixty years of widespread warming in the southern middle and high latitudes (1957–2016). Journal of Climate 2019;32(20):6875–6898.

[21] Kanamitsu M, Ebisuzaki W, Woollen J, Yang SK, Hnilo J, Fiorino M, et al. Ncep–doe amip-ii reanalysis (r-2). Bulletin of the American Meteorological Society 2002;83(11):1631–1644.

[22] Kostov Y, Marshall J, Hausmann U, Armour KC, Ferreira D, Holland MM. Fast and slow responses of Southern Ocean sea surface temperature to SAM in coupled climate models. Climate Dynamics 2017;48:1595–1609.

[23] Kuipers Munneke P, Luckman A, Bevan S, Smeets C, Gilbert E, Van den Broeke M, et al. Intense winter surface melt on an Antarctic ice shelf. Geophysical Research Letters 2018;45(15):7615–7623.

[24] Li G, Xie SP, Du Y. Monsoon-induced biases of climate models over the tropical Indian Ocean. Journal of Climate 2015;28(8):3058–3072.

[25] Li X, Cai W, Meehl GA, Chen D, Yuan X, Raphael M, et al. Tropical teleconnection impacts on Antarctic climate changes. Nature Reviews Earth & Environment 2021;2(10):680–698.

[26] Li X, Holland DM, Gerber EP, Yoo C. Impacts of the north and tropical Atlantic Ocean on the Antarctic Peninsula and sea ice. Nature 2014;505(7484):538–542.

[27] Long SM, Li G, Hu K, Ying J. Origins of the IOD-like biases in CMIP multimodel ensembles: The atmospheric component and ocean–atmosphere coupling. Journal of Climate 2020;33(24):10437–10453.

[28] Luo JJ, Zhang R, Behera SK, Masumoto Y, Jin FF, Lukas R, et al. Interaction between El Nino and extreme Indian ocean dipole. Journal of Climate 2010;23(3):726–742.

[29] Lyu K, Zhang X, Church JA. Regional dynamic sea level simulated in the CMIP5 and CMIP6 models: mean biases, future projections, and their linkages. Journal of Climate 2020;33(15):6377–6398.

[30] McKenna S, Santoso A, Gupta AS, Taschetto AS, Cai W. Indian Ocean Dipole in CMIP5 and CMIP6: characteristics, biases, and links to ENSO. Scientific reports 2020;10(1):1–13.

[31] Meehl GA, Arblaster JM, Bitz CM, Chung CT, Teng H. Antarctic sea-ice expansion between 2000 and 2014 driven by tropical Pacific decadal climate variability. Nature Geoscience 2016;9(8):590–595.

[32] Meehl GA, Arblaster JM, Chung CT, Holland MM, DuVivier A, Thompson L, et al. Sustained ocean changes contributed to sudden Antarctic sea ice retreat in late 2016. Nature communications 2019;10(1):14.

[33] Meier WN, Fetterer F, Windnagel AK, Stewart JS, NOAA/NSIDC Climate Data Record of Passive Microwave Sea Ice Concentration, Version 4. National Snow and Ice Data Center; 2021. `https://nsidc.org/data/G02202/versions/4`.

[34] Nuncio M, Yuan X. The influence of the Indian Ocean dipole on Antarctic sea ice. Journal of Climate 2015;28(7):2682–2690.

[35] Orr A, Deb P, Clem KR, Gilbert E, Bromwich DH, Boberg F, et al. Characteristics of surface “melt potential” over Antarctic ice shelves based on regional atmospheric model simulations of summer air temperature extremes from 1979/80 to 2018/19. Journal of Climate 2023;36(10):3357–3383.

[36] Paolo FS, Fricker HA, Padman L. Volume loss from Antarctic ice shelves is accelerating. Science 2015;348(6232):327–331.

[37] Parkinson CL. A 40-y record reveals gradual Antarctic sea ice increases followed by decreases at rates far exceeding the rates seen in the Arctic. Proceedings of the National Academy of Sciences 2019;116(29):14414–14423.

[38] Pritchard H, Ligtenberg SR, Fricker HA, Vaughan DG, van den Broeke MR, Padman L. Antarctic ice-sheet loss driven by basal melting of ice shelves. Nature 2012;484(7395):502–505.

[39] Purich A, England MH. Tropical teleconnections to Antarctic sea ice during austral spring 2016 in coupled pacemaker experiments. Geophysical Research Letters 2019;46(12):6848–6858.

[40] Rayner N, Parker DE, Horton E, Folland CK, Alexander LV, Rowell D, et al. Global analyses of sea surface temperature, sea ice, and night marine air temperature since the late nineteenth century. Journal of Geophysical Research: Atmospheres 2003;108(D14).

[41] Rignot E, Mouginot J, Scheuchl B, Van Den Broeke M, Van Wessem MJ, Morlighem M. Four decades of Antarctic Ice Sheet mass balance from 1979–2017. Proceedings of the National Academy of Sciences 2019;116(4):1095–1103.

[42] Saji N, Goswami BN, Vinayachandran P, Yamagata T. A dipole mode in the tropical Indian Ocean. Nature 1999;401(6751):360–363.

[43] Saji N, Yamagata T. Structure of SST and surface wind variability during Indian Ocean dipole mode events: COADS observations. Journal of Climate 2003;16(16):2735–2751.

[44] Sardeshmukh PD, Hoskins BJ. The generation of global rotational flow by steady idealized tropical divergence. Journal of the Atmospheric Sciences 1988;45(7):1228–1251.

[45] Senapati B, Deb P, Dash MK, Behera SK. Origin and dynamics of global atmospheric wavenumber-4 in the Southern mid-latitude during austral summer. Climate Dynamics 2022;59(5-6):1309–1322.

[46] Shu Q, Wang Q, Song Z, Qiao F, Zhao J, Chu M, et al. Assessment of sea ice extent in CMIP6 with comparison to observations and CMIP5. Geophysical Research Letters 2020;47(9):e2020GL087965.

[47] Simpkins GR, McGregor S, Taschetto AS, Ciasto LM, England MH. Tropical connections to climatic change in the extratropical Southern Hemisphere: The role of Atlantic SST trends. Journal of climate 2014;27(13):4923–4936.

[48] Simpkins GR, Peings Y, Magnusdottir G. Pacific influences on tropical Atlantic teleconnections to the Southern Hemisphere high latitudes. Journal of Climate 2016;29(18):6425–6444.

[49] Spence P, Griffies SM, England MH, Hogg AM, Saenko OA, Jourdain NC. Rapid subsurface warming and circulation changes of Antarctic coastal waters by poleward shifting winds. Geophysical Research Letters 2014;41(13):4601–4610.

[50] Stokes CR, Abram NJ, Bentley MJ, Edwards TL, England MH, Foppert A, et al. Response of the East Antarctic Ice Sheet to past and future climate change. Nature 2022;608(7922):275–286.

[51] Stuecker MF, Bitz CM, Armour KC. Conditions leading to the unprecedented low Antarctic sea ice extent during the 2016 austral spring season. Geophysical Research Letters 2017;44(17):9008–9019.

[52] Sun S, Fang Y, Zu Y, Liu L, Li K. Increased occurrences of early Indian Ocean Dipole under global warming. Science Advances 2022;8(47):eadd6025.

[53] Swetha Chittella SP, Deb P, Melchior van Wessem J. Relative Contribution of Atmospheric Drivers to "Extreme" Snowfall Over the Amundsen Sea Embayment. Geophysical Research Letters 2022;49(16):e2022GL098661.

[54] Taylor KE, Stouffer RJ, Meehl GA. An overview of CMIP5 and the experiment design. Bulletin of the American meteorological Society 2012;93(4):485–498.

[55] Thompson DW, Solomon S, Kushner PJ, England MH, Grise KM, Karoly DJ. Signatures of the Antarctic ozone hole in Southern Hemisphere surface climate change. Nature geoscience 2011;4(11):741–749.

[56] Tian B, Dong X. The double-ITCZ bias in CMIP3, CMIP5, and CMIP6 models based on annual mean precipitation. Geophysical Research Letters 2020;47(8):e2020GL087232.

[57] Turner J, Bracegirdle TJ, Phillips T, Marshall GJ, Hosking JS. An initial assessment of Antarctic sea ice extent in the CMIP5 models. Journal of Climate 2013;26(5):1473–1484.

[58] Turner J, Colwell SR, Marshall GJ, Lachlan-Cope TA, Carleton AM, Jones PD, et al. Antarctic climate change during the last 50 years. International journal of Climatology 2005;25(3):279–294.

[59] Turner J, Phillips T, Marshall GJ, Hosking JS, Pope JO, Bracegirdle TJ, et al. Unprecedented springtime retreat of Antarctic sea ice in 2016. Geophysical Research Letters 2017;44(13):6868–6875.

[60] Wang C, Zhang L, Lee SK, Wu L, Mechoso CR. A global perspective on CMIP5 climate model biases. Nature Climate Change 2014;4(3):201–205.

[61] Wang G, Cai W, Santoso A. Assessing the impact of model biases on the projected increase in frequency of extreme positive Indian Ocean dipole events. Journal of Climate 2017;30(8):2757–2767.

[62] Wang G, Cai W, Santoso A. Simulated thermocline tilt over the tropical Indian Ocean and its influence on future sea surface temperature variability. Geophysical Research Letters 2021;48(6):e2020GL091902.

[63] Wang G, Hendon HH, Arblaster JM, Lim EP, Abhik S, van Rensch P. Compounding tropical and stratospheric forcing of the record low Antarctic sea-ice in 2016. Nature communications 2019;10(1):13.

[64] Webster PJ, Moore AM, Loschnigg JP, Leben RR. Coupled ocean–atmosphere dynamics in the Indian Ocean during 1997–98. Nature 1999;401(6751):356–360.

[65] Xie P, Arkin PA. Global precipitation: A 17-year monthly analysis based on gauge observations, satellite estimates, and numerical model outputs. Bulletin of the american meteorological society 1997;78(11):2539–2558.

[66] Yu L, Zhong S, Vihma T, Sui C, Sun B. The Impact of the Indian Ocean Basin Mode on Antarctic Sea Ice Concentration in Interannual Time Scales. Geophysical Research Letters 2022;49(11):e2022GL097745.

[67] Yuan X. ENSO-related impacts on Antarctic sea ice: a synthesis of phenomenon and mechanisms. Antarctic Science 2004;16(4):415–425.

[68] Yuan X, Kaplan MR, Cane MA. The interconnected global climate system—A review of tropical–polar teleconnections. Journal of Climate 2018;31(15):5765–5792.

[69] Yuan X, Martinson DG. The Antarctic dipole and its predictability. Geophysical Research Letters 2001;28(18):3609–3612.

[70] Zhao M, Hendon HH. Representation and prediction of the Indian Ocean dipole in the POAMA seasonal forecast model. Quarterly Journal of the Royal Meteorological Society: A journal of the atmospheric sciences, applied meteorology and physical oceanography 2009;135(639):337–352.

**TABLE 1** CMIP classification

| | IOD precipitation pattern bias: small | IOD precipitation pattern bias: large |
|---|---|---|
| Waveguide bias: small | CLass A (CMIP5 (4): ACCESS 1.0, CanESM2, GFDL-CM3, CMCC-CESM. CMIP6 (7): ACCESS-CM2, CanESM5, CESM2, CESM2-FV2, CESM2-WACCM, MIROC6, MPI-ESM1-2-HR) | Class B (CMIP5 (6): ACCESS 1.3, CMCC-CMS, CNRM-CM5, HadGEM2-CC, HadGEM2-ES, MRI-ESM1. CMIP6 (11): BCC-ESM1, CESM2-WACCM-FV2, CNRM-CM6-1, FGOALS-f3-L, GFDL-CM4, GFDL-ESM4, INM-CM5-0, IPSL-CM6A-LR, MRI-ESM2-0, NorESM2-LM, UKESM1-0-LL) |
| Waveguide bias: large | Class C (CMIP5 (6): GFDL-ESM2M, HadCM3, IPSL-CM5A-MR, MIROC5, MIROC-ESM, MPI-ESM-MR. CMIP6(1): IITM-ESM) | Class D (CMIP5 (3): CMCC-CM, GFDL-ESM2G, MRI-CGCM3. CMIP6 (2): CNRM-CM6-1-HR, CNRM-ESM2-1.) |

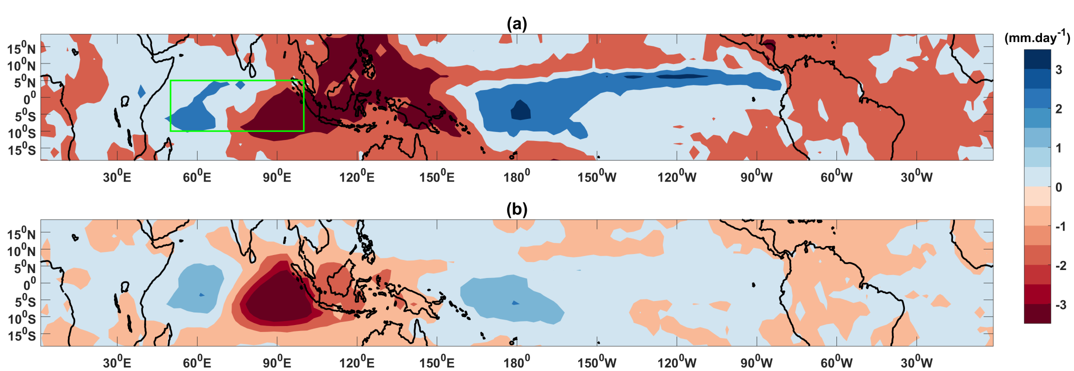


**FIGURE 1** (a) Composite map of daily precipitation anomaly from CMAP during SON of positive IOD years between 1980 and 2015. The green box represents the anomalous IOD precipitation dipole region. (b) Composite map of daily CMAP precipitation anomaly over days when similarity metric values were within the upper quartile.

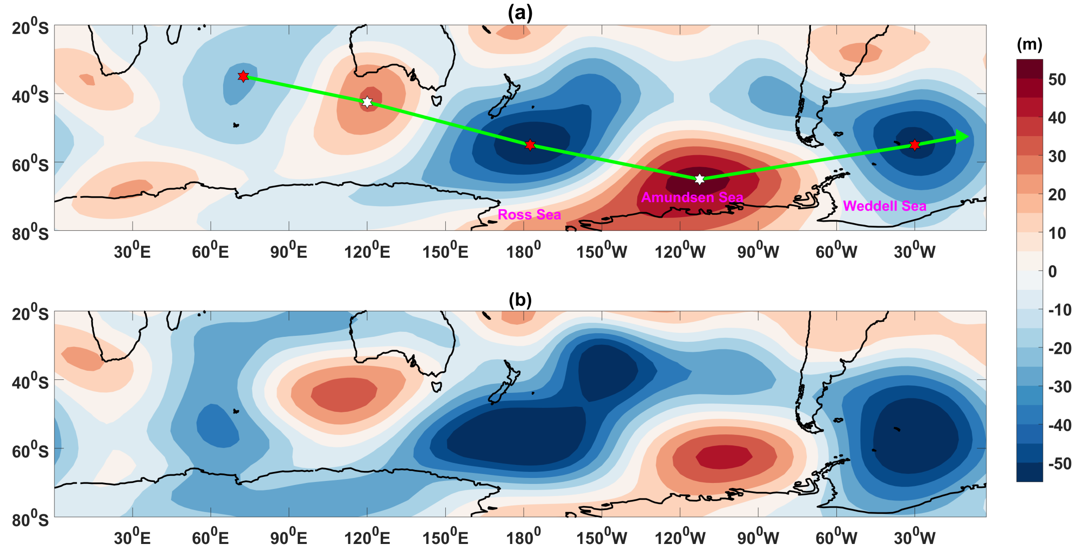


**FIGURE 2** (a) Step response function for anomalous 250-hPa geopotential height from NCEP-DOE Reanalysis II, averaged over lag 30-40 days, forced by 1 standard deviation of the similarity metric calculated from daily CMAP precipitation. The green arrow indicates the Rossby wave propagation path. White markers indicate the maxima of the positive anomaly centres, and red markers indicate the minima of the negative anomaly centres. (b) Composite map of anomalous 250-hPa geopotential height from NCEP-DOE Reanalysis II during SON of positive IOD years between 1980 and 2015.

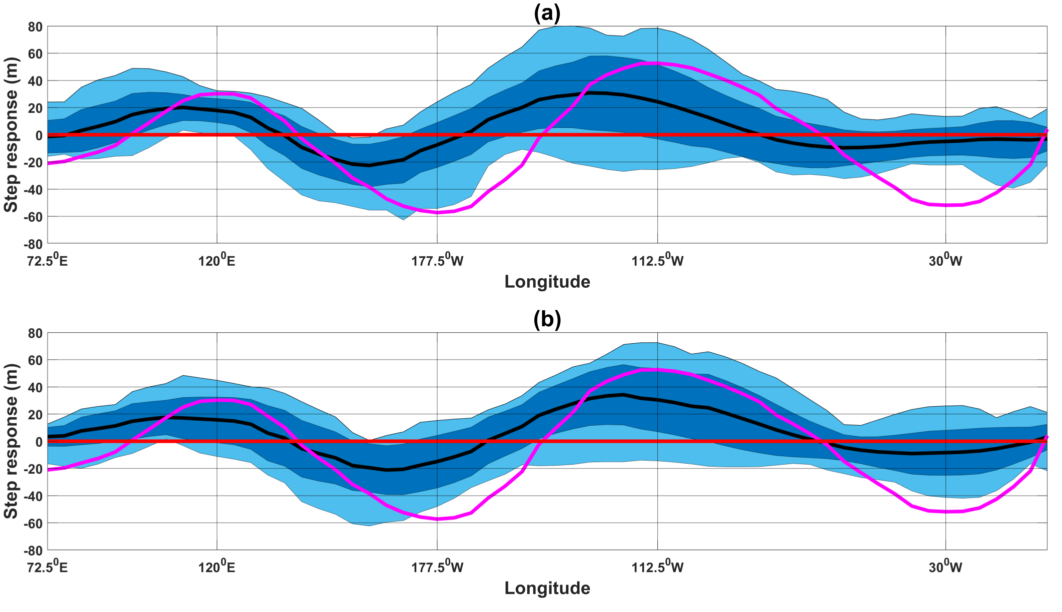


**FIGURE 3** Step response, averaged over 1000 km meridional distance at each longitude along the observed Rossby wave propagation path as shown in Figure 2a, for observation (magenta line), CMIP5 models (a), and CMIP6 models (b). The black line represents the multi-model mean from CMIP models, with a band of ±1 standard deviation given by the dark blue shading and the multi-model range provided by the light blue shaded region. The horizontal zero line is represented by red color.

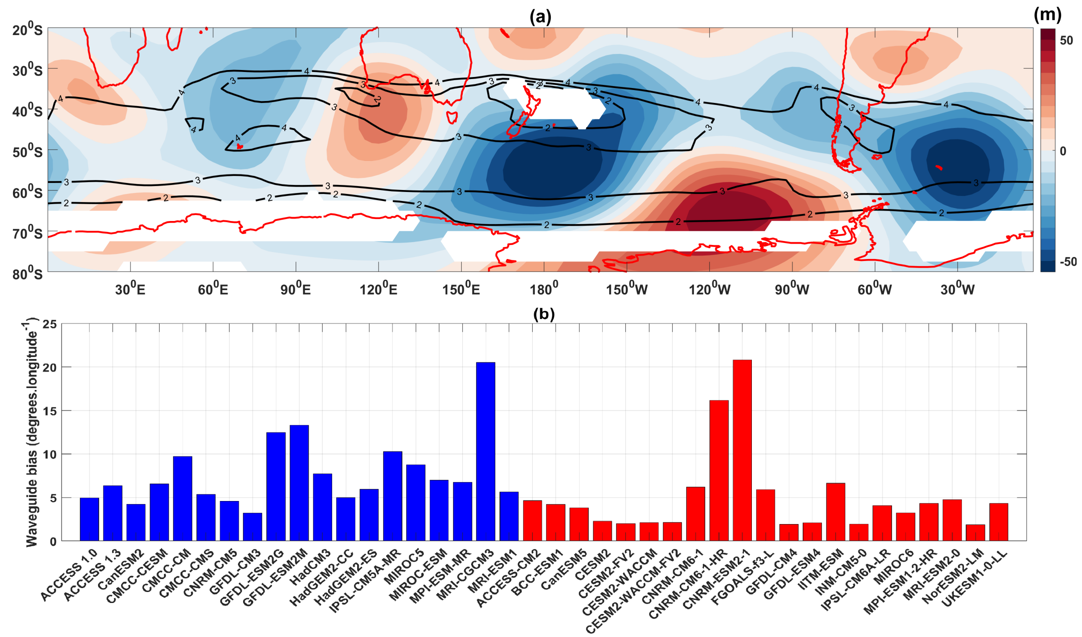


**FIGURE 4** (a) Step response function as in Figure 2a and stationary wavenumbers 2, 3 and 4 (black contours) computed from the time mean zonal wind at 250-hPa from NCEP-DOE Reanalysis II. Regions of easterly winds and reversed meridional absolute vorticity gradient where Rossby waves cannot propagate are masked. (b) Bar chart of the waveguide bias for the individual CMIP5 (blue) and CMIP6 (red) models.

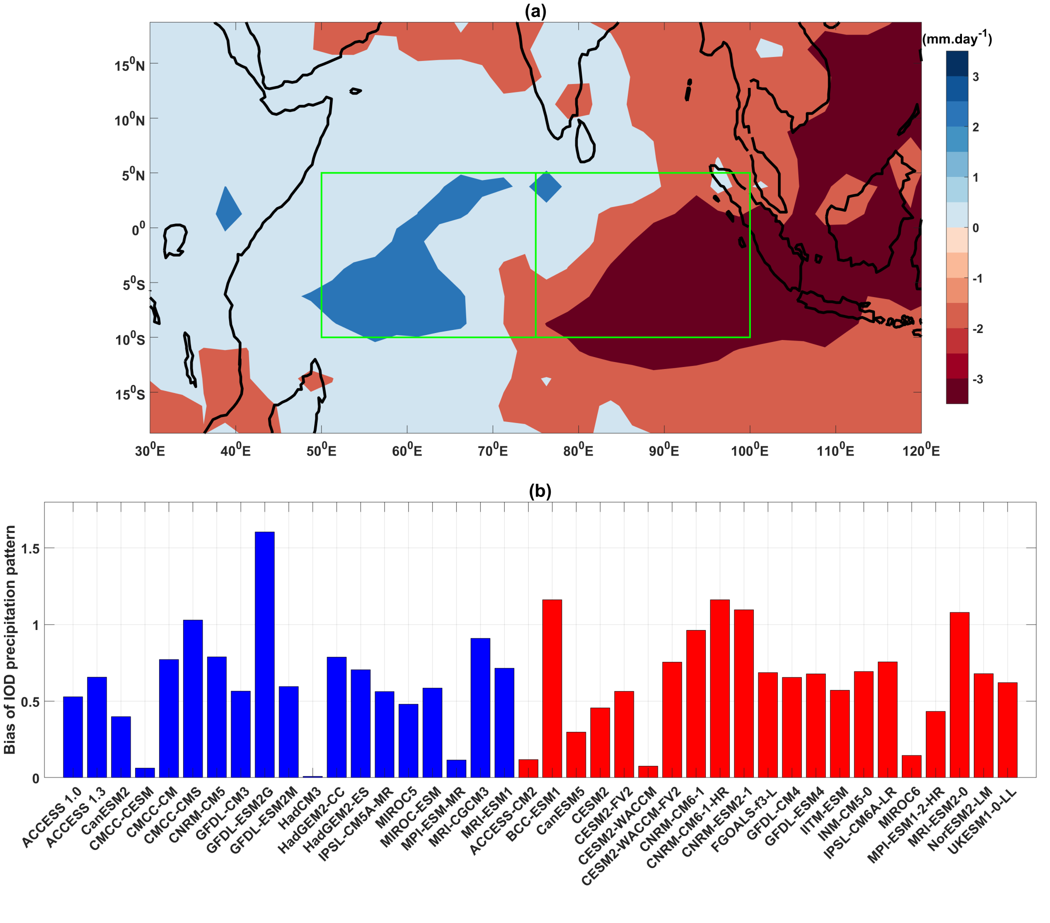


**FIGURE 5** (a) Composite map of daily precipitation anomaly from CMAP during SON of positive IOD years between 1980 and 2015. The green box was used to calculate the east-west ratio. (b) The Bar chart shows the IOD precipitation pattern bias for the individual CMIP5 (blue) and CMIP6 (red) models.

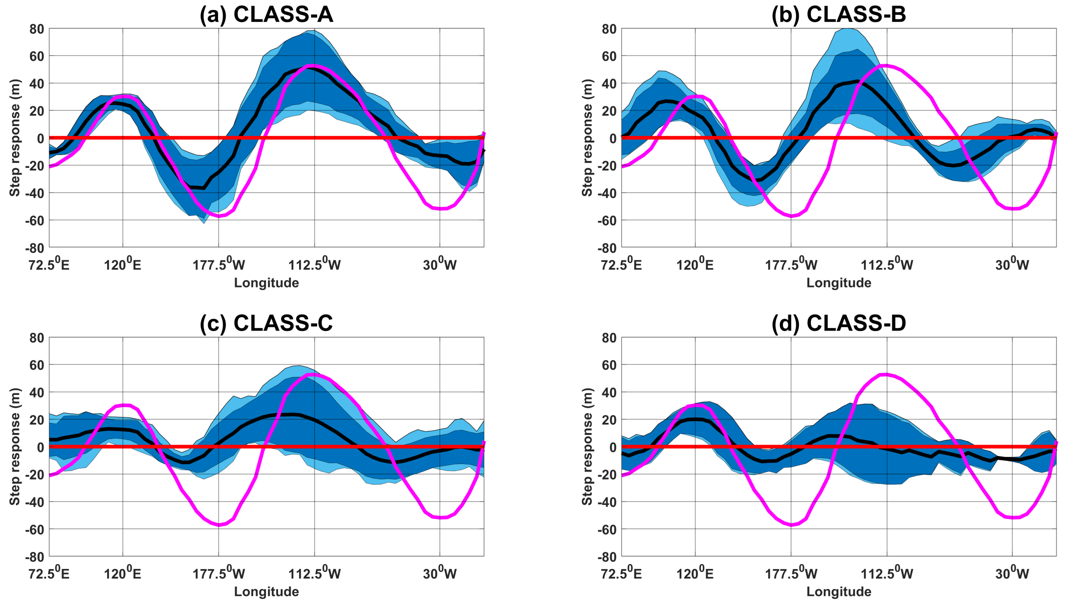


**FIGURE 6** Step response, averaged over 1000 km meridional distance at each longitude along the observed Rossby wave propagation path as shown in Figure 2a, for observation (magenta line) and CMIP5 classes. The black line represents the multi-model mean from each class, with a band of ±1 standard deviation given by the dark blue shading and the multi-model range provided by the light blue shaded region. The horizontal zero line is represented by red color.

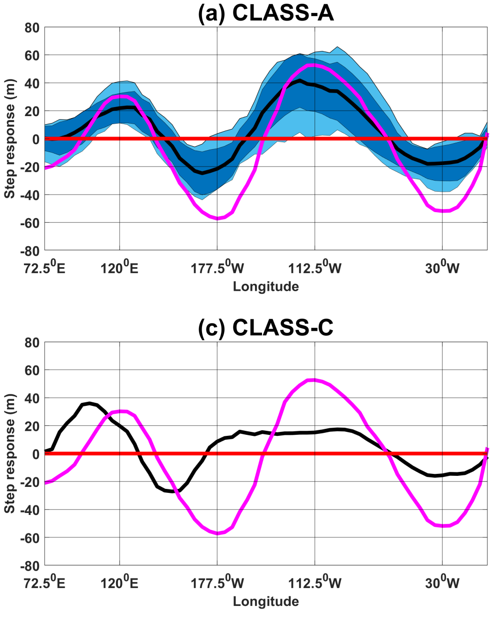


**FIGURE 7** Same as Figure 6 but for CMIP6 classes. In the case of class-C, the averaged step response is depicted in black color, and no multi-model range or ±1 standard deviation band is displayed since there is only one model within the class.

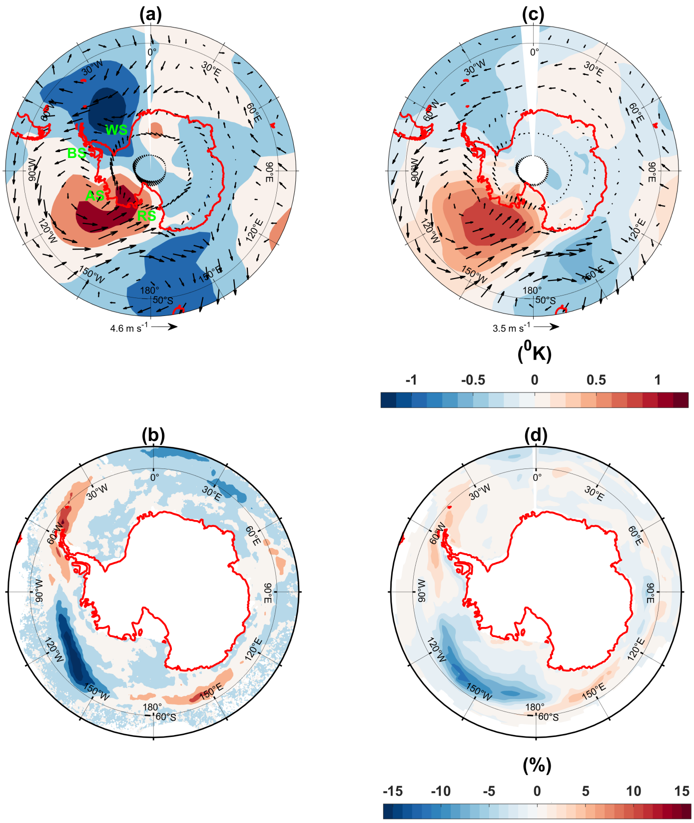


**FIGURE 8** Step response function for anomalous 850-hPa temperature and wind fields (black arrows), and anomalous sea ice concentration, averaged over lag 30-40 days, forced by 1 standard deviation of the similarity metric for observation (a, b), and ensemble of class-A models from CMIP5 (c, d) and CMIP6 (e, f). (RS: Ross Sea, AS: Amundsen Sea, BS: Bellingshausen Sea, WS: Weddell Sea)